C. R. Mecanique 342 (2014) 299–310

Contents lists available at ScienceDirect

Comptes Rendus Mecanique

www.sciencedirect.com

Frontiers of micro and nanomechanics of materials: Soft or amorphous matter, surface effects

Experimental investigation and modelling of compressibility induced by damage in carbon black-reinforced natural rubber

Sabine Cantournet *, Khaled Layouni, Lucien Laiarinandrasana, Roland Piques

Centre des matériaux, CNRS UMR 7633, MINES ParisTech, BP 87, 91003 Évry cedex, France

ARTICLE INFO

Article history:
Received 27 August 2013
Accepted 10 December 2013
Available online 10 May 2014

Keywords:
Rubber
Compressibility
Cavitation
Damage
Constitutive behaviour
Finite element method

ABSTRACT

While natural rubber is commonly considered as an incompressible material, this study shows how carbon black-reinforced natural rubber (NR-CB), when subjected to various mechanical loading conditions (uniaxial, hydrostatic, monotonic, cyclic), is affected by volume change. Experiments show a volume variation even for low straining values and a significant volume change for large elongations. Moreover, volume change can be either reversible or not, depending on the loading conditions. It is related to a competition between void growth, chain orientation, and stress softening. At a microscopic scale, in situ Scanning Electron Microscopy (SEM) examinations and image analysis allow one to record damage and microscopic volume change as a function of elongation. Therefore the volume change measured at the microscopic scale is equal to the macroscopic one. Based on the experimental results, this paper shows that the hypothesis of incompressibility is worth being revisited. Thus, a nearly compressible approach was considered, where the strain energy is assumed to be the sum of spherical and deviatoric parts that are both affected by damage. The model was then implemented in a finite-element code. Good agreement was obtained between experimental results and model predictions for low triaxiality test conditions.

0. Introduction

The shear modulus of natural rubber varies with temperature and straining. Commonly reported values lay between 0.5 and 6 MPa. On the other hand, the bulk modulus is generally assumed to be strain independent and can reach a value as high as 1000 MPa. Due to the high ratio between bulk modulus and shear modulus, natural rubber is usually assumed to be nearly incompressible. Constitutive modelling commonly used to describe the behaviour of carbon black-filled natural rubber uses an incompressible constraint assumption.

To the authors' knowledge, Busse [1] and Yerzley [2] were the first to find internal rupture of rubber subjected to hydrostatic tensile stress. According to Gent & Lindley [3], the critical stress value that initiates cavitation is related to the elastic characteristics of rubber. Later, Gent & Tompkins [4], who used a dissolved gas to identify the onset of cavitation, showed that this critical value is about $5G/2$, where G is the rubber's shear modulus. This result was confirmed by Cho & Gent [5] and by Gent & Wang [6]. Accordingly, cavitation that leads to volume change in rubber has mainly been studied under hydrostatic tensile loading [7–9]. The present paper aims at studying volume change under various loading conditions. The carbon black-filled natural rubber (NR-CB) material under study exhibits several phenomena affecting volume change,

* Corresponding author. Tel.: +33 (0)1 60 76 30 52; fax: +33 (0)1 60 76 31 50.
E-mail address: sabine.cantournet@mines-paristech.fr (S. Cantournet).

http://dx.doi.org/10.1016/j.crme.2014.02.005
1631-0721/

Table 1
General formulation of the carbon black-reinforced natural rubber used in the study.

Ingredient	Wt% (with respect to NR)	Volume fraction (%)
NR	100	75
Sulphur	1–2	0.3–0.7
ZnO	10^{-2}	11.8
CB	23	8.7

Table 2
Mechanical properties of NR-CB used in the study.

Density (g/cm^3)	1.1
Hardness (shore)	48
Failure stress in tension (MPa)	25.3
Failure strain in tension (%)	500
Tangent modulus at 300% in tension (MPa)	7.8

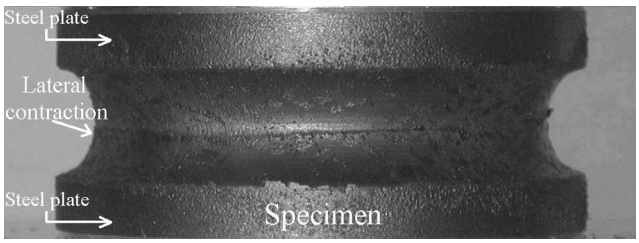

Fig. 1. "Pancake specimen" used for hydrostatic test: lateral contraction.

namely crystallisation, stress softening, and damage. Damage leads to an increase in volume, whereas both stress softening [10] and crystallisation [11–13] induce a volume decrease. In fact, when crystallisation occurs, the chains are aligned and the material is compacted.

The paper presents an experimental investigation of the volume change of an NR-CB material under various loading conditions, both from a macroscopic and a microscopic point of view. Then, a damage-induced compressibility model is presented; finite-element calculations using this model are compared to our experimental results.

1. Material and experimental techniques

1.1. Material

The material of interest is a *cis*-1,4-polyisoprene reinforced by carbon black and is essentially used for bearings subjected to fatigue. Its chemical composition and mechanical properties are shown in Table 1 and Table 2, respectively. Note the large amount of ZnO introduced in the material compared to the literature data. Its influence on volume change will be discussed later.

1.2. Mechanical testing

Uniaxial tests were carried out using a universal tensile machine. The specimens are 2 mm thick and 6 mm wide thin strips. Monotonic tensile tests were performed at a constant engineering strain rate (displacement rate divided by specimen gauge length) laying between 10^{-3} s^{-1} and 5×10^{-2} s^{-1}, whereas cyclic loading tests were carried out at constant engineering strain rate equal to 10^{-2} s^{-1}.

For uniaxial compression, the specimens are cylindrical and have a diameter of 19 mm and a height of 8 mm. They have been lubricated in order to avoid friction. Tests were also performed at different engineering strain rates within the range of 3.5×10^{-2} s^{-1}–1.6×10^{-1} s^{-1}.

The oedometric compression consists in testing a cylindrical specimen under compression within a rigid chamber. The specimens have a diameter of 19 mm and a height of 8 mm and were also lubricated in order to avoid friction. Several engineering strain rates were applied ranging from 0.8×10^{-4} s^{-1} to 3.8×10^{-2} s^{-1}.

For hydrostatic loading, the experimental device consists of an electromechanical machine with a load capacity of 100 kN and a crosshead-speed ranging from 100 to 500 mm min^{-1}. The specimen used for this kind of loading consists of thin disk rubber layers attached by vulcanisation to top and bottom steel grips (Fig. 1). These cylindrical "pancake specimens" have a diameter of 40.6 mm and are 3 mm high. Tests were carried out under monotonic and cyclic loading. Engineering strain rates range from 10^{-1} s^{-1} to 10^{-3} s^{-1}.

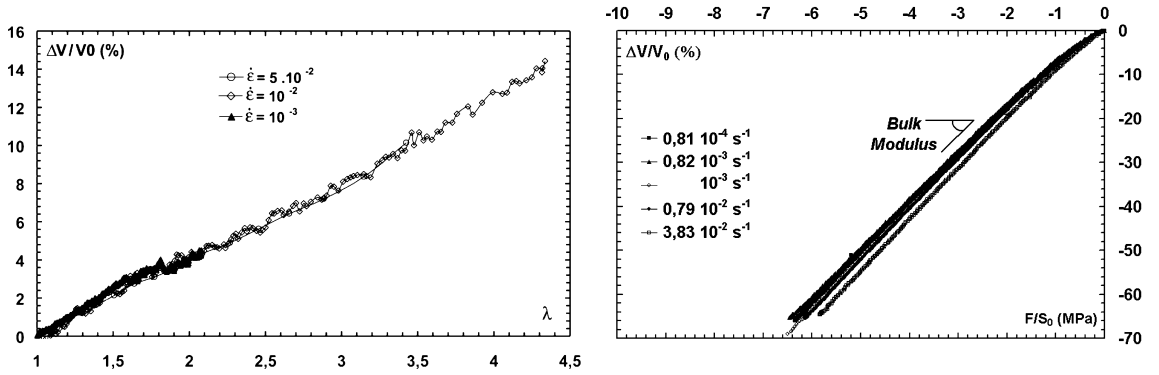

Fig. 2. (a) Volume change under tension compression at various engineering strain rates, (b) volume change under oedometric at various engineering strain rates.

Finally, in situ SEM uniaxial tension experiments were performed using a thin strip and a low acceleration voltage of about 1 kV.

1.3. Volume change measurement

The experimental device used for volume change quantification under uniaxial loading is called Video Traction™. The principle consists in following, by means of a CCD camera, the displacement and distortion of seven full circles initially drawn on the surface of the specimen. Dashes are circular, have a diameter of approximately 1 mm and are 0.25 mm distant. Further information about Video Traction™ experimental device is given in [14]. The volume is then measured thanks to the determination of principal Hencky strain $h_{11} = \ln(\lambda_{11})$ and $h_{22} = \ln(\lambda_{22})$ and the isotropy assumption, such that

$$\frac{\Delta V}{V_0}(\%) = \left(e^{(h_{11}+2\cdot h_{22})} - 1\right)\cdot 100 \tag{1}$$

where λ_{11}, λ_{22} are the longitudinal and transverse elongation respectively and $\lambda = \frac{L}{L_0}$, L and L_0 are the present and the initial specimen lengths.

Under uniaxial compression, images of the specimen are tracked during loading, which gives its shape evolution. This allows us, as the specimen is axisymmetric, to quantify volume change under uniaxial compression. The ratio between the diameter and the height of a "pancake specimen" allows us to ensure a hydrostatic stress state in the centre. The observation of the specimen during loading shows the occurrence of an edge effect (Fig. 1). The actual volume change was then determined by taking into account the axial stretch given by displacement sensors and the lateral contraction by means of a video-controlled device.

2. Experimental results

The compressibility of the material was first characterised by carrying out an oedometric compression. This test allows us to apply a negative high-stress triaxiality at low strains. Next, volume change was measured for low-stress triaxiality under uniaxial tensile test. As the material is used for fatigue, volume change was measured under cyclic loading. So as to detect the microscopic phenomena responsible for volume change, in situ SEM uniaxial tension experiments have been performed. In order to establish the effect of a highly positive stress triaxiality onto volume change, hydrostatic tests were performed under monotonic and cyclic loading. Furthermore, volume change was characterised under uniaxial and hydrostatic compressions. All the specimens surfaces were then observed by means of optical microscopy and SEM.

2.1. Oedometric compression

The slopes of all curves are independent of the strain rate in the range studied (Fig. 2) and correspond to the bulk modulus (K_v) which is about 1130 MPa. This value is in agreement with those of other elastomeric materials tested with the same conditions such as silica-filled natural rubber (1200 MPa and 1265 MPa), EPDM (1600 MPa) and silica-filled SBR (1900 MPa). The value of shear modulus (G) is about 1 MPa. Due to the high ratio between these two moduli (K_v and G), this material can be considered to be **initially** quasi-incompressible.

2.2. Uniaxial tension

When stretched monotonically until a maximum strain of $\lambda = 4.2$, the material response reveals three important aspects of the macroscopic volume change $(\Delta V/V_0)_{\text{Macro}}$, as shown in Fig. 2a and Fig. 3a: (i) it is engineering-strain-rate inde-

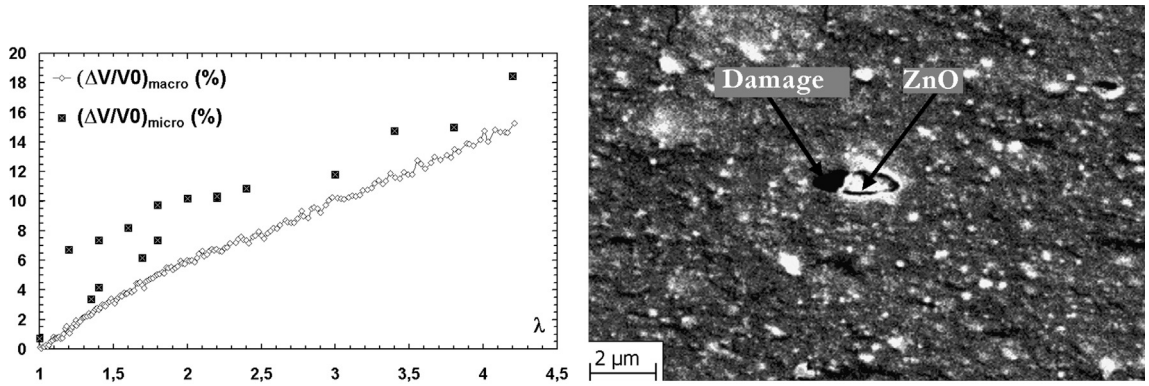

Fig. 3. Uniaxial tension. (a) Macroscopic and microscopic volume change with respect to elongation. (b) Identification of the ZnO particles responsible for microscopic cavitation (in situ tension along the horizontal direction).

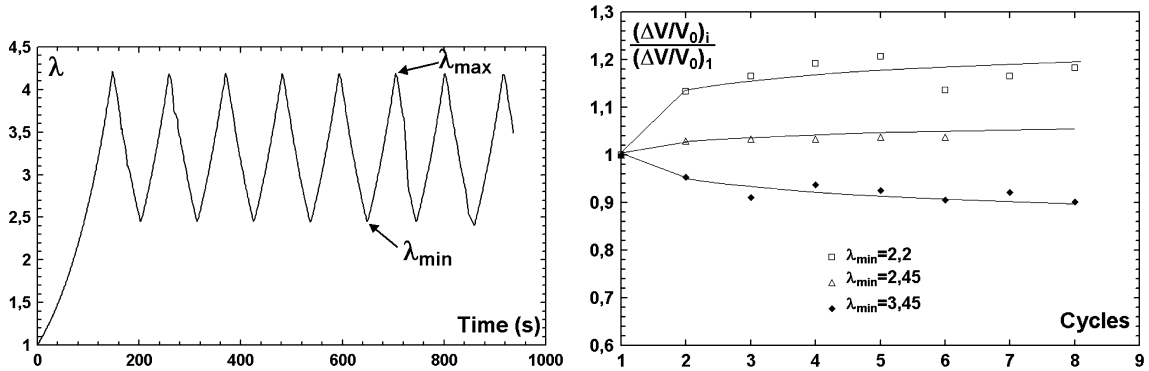

Fig. 4. (a) First series of cyclic uniaxial tension tests. (b) Relative volume change $(\Delta V/V_0)_{ith}$ cycle/$(\Delta V/V_0)_{1st}$ cycle at $\lambda = \lambda_{min}$ versus cycle number under cyclic loading for $\lambda_{max} = 4.2$ and various values of λ_{min}.

pendent, (ii) it occurs even at low elongation values ($\lambda = 1.1$): i.e. no threshold, (iii) its value can be as high as 15% for $\lambda = 4.2$.

At the microscopic scale (in situ tension), voids appear as soon as the material is stretched. So no elongation threshold exists for cavitation as it was already observed at the macroscopic scale. Then, ZnO particles have been systematically detected in the neighbourhood of cavitated areas (Fig. 3b). So, their distribution in the material and the evolution of their shape ratio have been determined. ZnO particles are spherical and isotropically distributed in the material. Recent tests under x-ray were unable to confirm the isotropic or near-isotropic assumption [15]. This result allows us to assume that the surface fraction (quantification made in 2D) is equal to the volume one (3D result). By means of image analysis, the evolution of the microscopic volume is measured (ratio between the void surface and the examined area) as a function of elongation. The examined area was obtained by cartography and its size is about 350 μm by 350 μm. It comes out that, under uniaxial tension, the microscopic volume change $(\Delta V/V_0)_{Micro}$ is slightly higher than the macroscopic one (Fig. 3a). This could be due to the difference between the two test conditions and the image analysis errors. Thus, macroscopic and microscopic volume changes should be considered as similar. In this study, the large amount of ZnO appears to be responsible for the initiation of volume change under uniaxial tension. In addition, when the specimen is unloaded, some cavitated areas are still present. So volume change could be distinguished into an irreversible part and a reversible one. Furthermore, uniaxial cyclic loading tests have been carried out. The first cyclic loading schedule consists in keeping constant the maximum elongation value ($\lambda_{max} = 4.2$) and by changing alternatively the minimum elongation (λ_{min}). By varying λ_{min} from 1.2 to 3.95, three trends can be evidenced for volume change at $\lambda = \lambda_{min}$, as exemplified in Fig. 4:

(1) for $\lambda_{min} \leqslant 2.2$, the minimum volume increases with increasing the number of cycles, corresponding mainly to damage accumulation during cycles. In fact, when the specimen is unloaded down to a minimum elongation value less than 2.2, strain-induced crystallisation vanishes (see [28]). In addition, in this case, stress softening does not play a significant role. So only damage appears to be responsible for the volume increase at λ_{min} for $\lambda_{min} \leqslant 2.2$;
(2) for $3.45 \leqslant \lambda_{min}$: increasing λ_{min} induces both permanent crystallisation and stress softening. Therefore crystallisation and stress softening effects become more important than damage ones, leading to a global cyclic volume decrease at λ_{min};

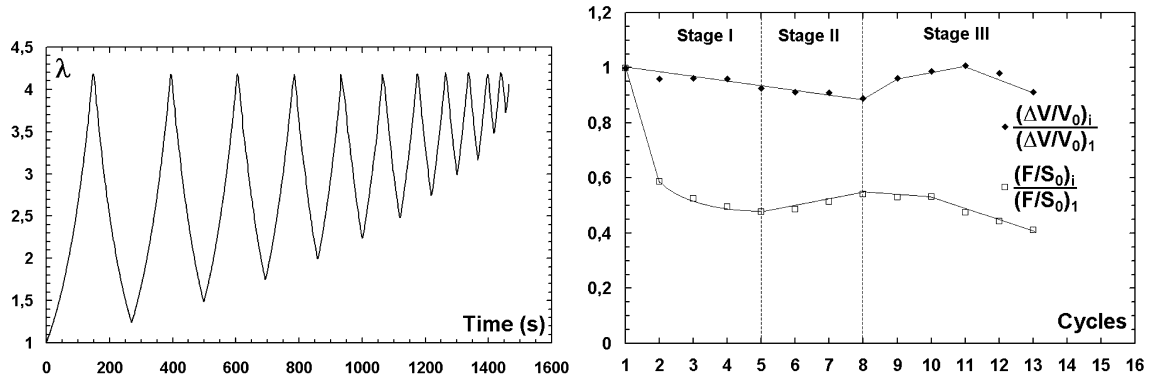

Fig. 5. (a) Second series of uniaxial cyclic tension tests. (b) Evolution of relative nominal stress, $(F/S_0)_{ith}$ cycle/$(F/S_0)_{1st}$ cycle at $\lambda = \lambda_{max}$ and relative volume change $(\Delta V/V_0)_{ith}$ cycle/$(\Delta V/V_0)_{1st}$ cycle at $\lambda = \lambda_{max}$ with cycles where $\lambda_{max} = 4.2$ and $1.2 < \lambda_{min} < 4.2$.

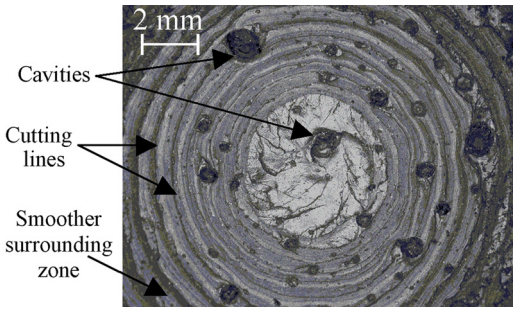

Fig. 6. Cross section perpendicular to the loading axis of a pancake specimen loaded in tension: a central damaged zone with spherical cavities with "onion-skin" topography and a smoother surrounding zone.

(3) for $2.2 < \lambda_{min} < 3.45$: the cyclic curve is identical to the first loading one. So, damage accumulation seems to be compensated by stress softening and crystallisation effects.

Another loading schedule was applied to confirm the competition between damage, crystallisation and stress softening. It consists in keeping λ_{max} constant and increasing the value of λ_{min} (Fig. 5). This test has been reproduced several times (10 times). The minimum volume change and minimum nominal stress increase during the cycles, whereas the maximum nominal stress (i.e. at $\lambda = \lambda_{max}$) behaves according to three stages:

(1) cycles 1–5 ($\lambda_{min} \leqslant 2.2$): the maximum nominal stress decreases due to stress softening;
(2) cycles 5–8 ($2.2 < \lambda_{min} < 2.95$): the minimum elongation reaches the threshold corresponding to the beginning of strain-induced crystallisation. That leads to an increase in the maximum nominal stress by crystallisation reinforcement;
(3) cycles 8–12 ($\lambda_{min} \geqslant 2.95$): crystallisation saturates, leading to a decrease in the maximum nominal stress by stress softening.

According to the maximum nominal stress evolution, volume change is expected to decrease by crystallisation and stress-softening effects. It is the case during the two first stages ($\lambda_{min} < 2.95$). Therefore, during the third stage, the maximum volume variation increases from the 8th to the 11th cycle ($2.95 \leqslant \lambda_{min} \leqslant 3.7$) before decreasing at $\lambda_{min} \leqslant 3.7$. This is due to damage effects that overcome crystallisation and stress softening ones. This result confirms the competition between damage, crystallisation, and stress softening.

From the results of these tests, keeping λ_{max} constant makes the stabilised volume change depend on the competition between damage accumulation, stress softening contribution, and strain-induced crystallisation effects. So, either a reversible evolution (steady-state volume variation during cycles) or an irreversible one (cyclic volume change increase or decrease from one cycle to the next one) may happen.

2.3. Hydrostatic tensile tests

By imposing elongation rates from 10^{-3} s^{-1} to 10^{-1} s^{-1}, no influence of the engineering strain rate on volume change could be checked. A transition concerning cavitation-induced damage appears at a nominal stress equal to 0.8 MPa and agrees with the work of Gent and Lindley [3]. Volume change is important as it reaches a value of 150% at $\lambda = 2.8$. Sectioning the specimen perpendicular to its axis (see cutting lines in Fig. 6) shows a central damaged zone with circular

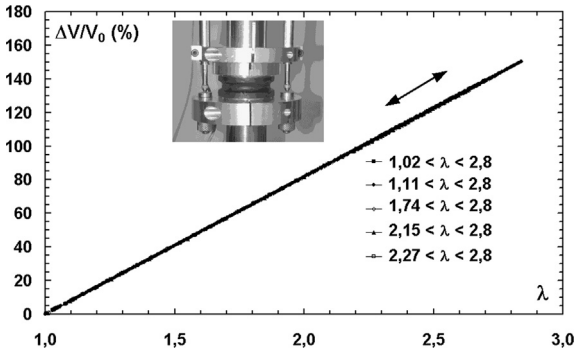

Fig. 7. Volume change versus elongation under cyclic loading of pancake specimens such that $\lambda_{max} = 2.8$ and λ_{min} is constant: $\lambda_{min} = 1.02, 1.11, 1.74, 2.15, 2.27$.

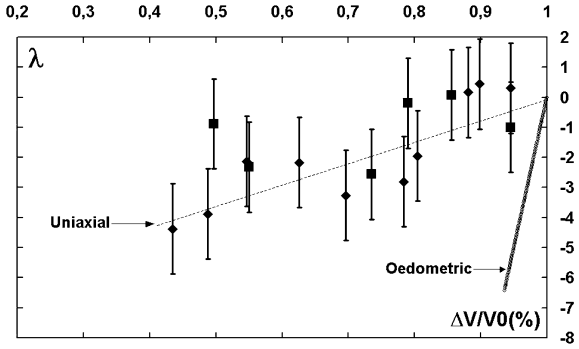

Fig. 8. Volume change with respect to elongation under uniaxial compression. Comparison with oedometric volume change.

cavities and a smoother surrounding zone. The location of circular cavities depends on the quasi-hydrostatic stress state at the centre, which vanishes at the periphery of the sample, giving rise to a deformation gradient. The observed cavities can lead, after coalescence, to the rupture of the specimen.

The damage mechanisms taking place for low cycles could be distinguished into two mechanisms: low- and high-triaxiality conditions. Under low-triaxiality loading, debonding between ZnO particles and matrix is responsible for cavitation. At the same time, nothing occurs in the neighbourhood of carbon black (CB) particles. This is due to the poor bonding between the matrix and the ZnO particles, whereas CB particles are well-bonded to the matrix because of their chemical and physical structure. Under hydrostatic loading, the damage is not related to ZnO particles location and is more pronounced, with an important number of 1-mm-size damaged zones. The mechanism is different from the former one and comes from the high-stress triaxiality that induces a sudden appearance of cavities, which is followed by crack propagation and coalescence. The aim of this paper is to model cavitation effects but not tearing ones, so only ZnO-matrix debonding will be taken into account. Consequently, only low triaxiality tests will be modelled.

The behaviour under cyclic hydrostatic loading has been studied at a controlled strain rate of 10^{-2} s^{-1}. The first series of cycles performed for uniaxial tests (Fig. 4a) were also applied on pancake specimens. The result differs from those obtained under uniaxial loading. In fact, volume change under uniaxial tension can either increase or decrease cyclically, depending on the minimum elongation value, whereas volume change under hydrostatic tension follows a steady-state evolution (Fig. 7) and depends neither on the minimum nor on the maximum elongation. Thus, volume change under hydrostatic conditions is totally controlled by growth and closure of cavities.

2.4. Uniaxial and hydrostatic compression

Volume change under uniaxial compression decreases due to the compaction of the material (Fig. 8). This decrease is lower than under oedometric conditions: this confirms that volume change is triaxiality dependent. Under hydrostatic compression, volume change is very low and strain rate independent (Fig. 9). Under low stress values, volume change is higher under oedometric loading than under hydrostatic loading, which confirms the volume-change triaxiality dependence. Moreover, sectioning the specimen perpendicular to its axis did not reveal any cavity. So no macroscopic effect of damage is assumed to occur in compression. To confirm this result, specimens have been loaded in tension after loading–unloading in compression. Loading–unloading paths in compression are similar and no difference could be observed between volume change obtained under tensile tests after and without previous loading–unloading in compression.

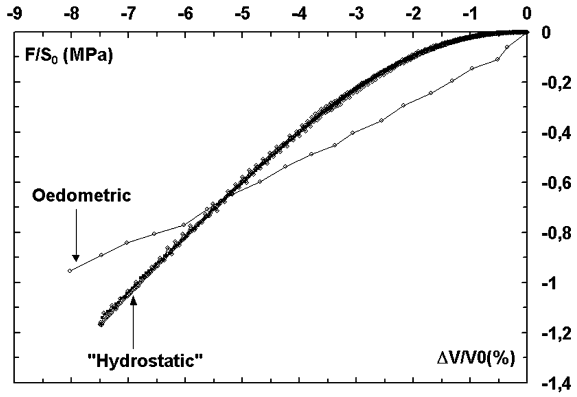

Fig. 9. Volume change with respect to nominal stress during hydrostatic compression. Influence of strain rate on volume change. Comparison with oedometric compression.

The previously described tests allow us to analyse the volume change under various kinds of loading. Under both uniaxial and hydrostatic compressions, the volume decreases due to material compaction and remains very low compared to tensile loading [16]. The increase in volume is much higher under hydrostatic tension than under uniaxial tension. This is due to the difference in stress triaxiality between the two loading conditions and shows that volume change is triaxiality dependent.

3. Modelling

As damage mechanisms differ from hydrostatic to uniaxial loading, only low triaxiality test conditions will be modelled, i.e. only cavitation induced by damage will be modelled. Also, stress softening and crystallisation effects are neglected: only the stabilised state obtained at the fifth cycle will be considered. So compressibility induced by damage was taken into account in a constitutive model. A phenomenological approach was chosen within the hyperelastic nearly compressible framework proposed by [17].

3.1. Model basis

In order to write the potential W in its volume-shear separable form, the [18] kinematic split is applied to the deformation gradient $\mathbf{F}$ as follows:

$$\mathbf{F} = \mathbf{F}^{\text{vol}} \cdot \bar{\mathbf{F}} \tag{2}$$

where $\mathbf{F}^{\text{vol}} = J^{1/3}\mathbf{I}$ is the volumetric deformation gradient tensor, J is the determinant of the deformation gradient tensor $\mathbf{F}$, $\mathbf{I}$ is the identity tensor and $\bar{\mathbf{F}}$ is the isochoric deformation gradient tensor. Every overlined quantity will refer to the isochoric part.

Consequently, volumetric and isochoric right Cauchy–Green tensors $\mathbf{C}^{\text{vol}}$ and $\bar{\mathbf{C}}$ are defined as

$$\mathbf{C}^{\text{vol}} = J^{2/3}\mathbf{I} \quad \text{and} \quad \bar{\mathbf{C}} = J^{-2/3}\mathbf{C} = \bar{\mathbf{F}}^{\mathbf{T}} \cdot \bar{\mathbf{F}}$$

The description is developed in a total Lagrangian frame. The internal free energy is assumed to be the sum of a deviatoric part and of a volumetric one, so that

$$W = W^{\text{iso}} + W^{\text{vol}} = (1-D)W_0(\bar{\mathbf{E}}) + K_{\text{v}}\psi(\tilde{J}) \tag{3}$$

where superscript iso (resp. vol) stands for the isochoric (resp. volumetric) part, D is the damage parameter ($0 \leqslant D < 1$), W_0 is the isochoric energy of the damage-free material, $\bar{\mathbf{E}}$ is the isochoric Green–Lagrange deformation tensor, K_{v} is the bulk modulus, $\tilde{J}$ is an effective value of J referring to the damage-free rubber gum and is related to the volume-change ratio J through the damage parameter D (Eq. (4)), and α is a positive parameter that allows one to distinguish the reversible volume change part from the irreversible one. In fact, when $\alpha = 1$, the volume variation is totally irreversible:

$$\tilde{J} = \frac{J}{g(D)} = \frac{J}{1+\alpha D} \tag{4}$$

By assuming that there is no heat exchange and by considering only intrinsic dissipation, the Clausius–Duhem inequality can be written as follows:

$$\left[\mathbf{S} - 2J^{-2/3}(1-D)\,DEV\left[\frac{\partial W_0}{\partial \bar{\mathbf{C}}}\right] - 2K_{\text{v}}\frac{\partial \psi(\tilde{J})}{\partial J}\frac{\partial J}{\partial \mathbf{C}}\right] : \dot{\mathbf{C}} + Y\dot{D} \geqslant 0 \tag{5}$$

where $\mathbf{S}$ is the second Piola–Kirchhoff stress tensor, $\mathbf{C} = \mathbf{F}^{\mathrm{T}} \cdot \mathbf{F}$ is the right Cauchy–Green tensor corresponding to the deformation gradient tensor $\mathbf{F}$, DEV is the deviatoric operator as defined by [19] (Eq. (6)), Y is the damage thermodynamic force (Eq. (7)) and $\dot{D}$ describes the damage rate:

$$DEV[\cdot] = [\cdot] - \frac{1}{3}\big([\cdot] : [\mathbf{C}]\big)\mathrm{C}^{-1} \tag{6}$$

$$Y = -\frac{\partial W}{\partial D} \tag{7}$$

The expression of Piola–Kirchhoff tensor (Eq. (8)) and the damage thermodynamic force (Eq. (9)) are then written as:

$$\mathbf{S} = \mathbf{S}^{\mathrm{iso}} + \mathbf{S}^{\mathrm{vol}} = 2J^{-2/3}(1-D)\,DEV\left[\frac{\partial W_0}{\partial \bar{\mathbf{C}}}\right] + 2K_{\mathrm{v}}\frac{\partial \psi(\tilde{J})}{\partial J}\frac{\partial J}{\partial \mathbf{C}} \tag{8}$$

$$Y = Y^{\mathrm{iso}} + Y^{\mathrm{vol}} = W_0 + \frac{K_{\mathrm{v}}}{2}\left(\frac{g'(D)}{g(D)}\right)\big(\tilde{J}^2 - 1\big) \tag{9}$$

where $g'(D) = \frac{\partial g}{\partial D}$.

By taking the isotropy assumption into account, the right Cauchy–Green tensor $\mathbf{C}$ can be represented by its invariants I_1, I_2 and I_3 defined as $I_1 = \mathrm{tr}(\mathbf{C})$, $I_2 = \frac{1}{2}[(\mathrm{tr}(\mathbf{C}))^2 - \mathrm{tr}(\mathbf{C}^2)]$ and $I_3 = \det(\mathbf{C})$.

Considering the isochoric right Cauchy–Green tensor $\bar{\mathbf{C}}$, the invariants are expressed as

$$\bar{I}_1 = \mathrm{tr}(\bar{\mathbf{C}}) = I_1 \cdot I_3^{-1/3} \tag{10}$$

$$\bar{I}_2 = \frac{1}{2}\big[\big(\mathrm{tr}(\bar{\mathbf{C}})\big)^2 - \mathrm{tr}\big(\bar{\mathbf{C}}^2\big)\big] = I_2 \cdot I_3^{-2/3} \tag{11}$$

where $\bar{I}_1$, $\bar{I}_2$ are the Penn invariants [20]. Then, a Rivlin form for W_0 has been chosen such that

$$W_0 = C_{10}(\bar{I}_1 - 3) + C_{01}(\bar{I}_2 - 3) + C_{20}(\bar{I}_1 - 3)^2 \tag{12}$$

where C_{10}, C_{01} and C_{20} are material parameters. Penn invariants allow one to force W_0 to be zero when the material is subjected to pure spherical loading. For the spherical strain energy, a quadratic form respecting [21] conditions has been chosen:

$$\psi(\tilde{J}) = \frac{1}{2}\left[\frac{1}{2}\big(\tilde{J}^2 - 1\big) - \log \tilde{J}\right] \tag{13}$$

Damage evolution is determined by defining a non-damage surface $f(Y, Q)$ such that

$$f(Y, Q) = Y - Q(D) \leqslant 0 \tag{14}$$

The following form of $Q(D)$ has been adopted with no damage threshold as observed experimentally:

$$Q(D) = \begin{cases} \eta(\ln(D_\infty) - \ln(D_\infty - D)) & \text{if } D < D_\infty \\ +\infty & \text{if } D = D_\infty \end{cases} \tag{15}$$

where η and D_∞ are material parameters. The maximum value of D is D_∞.

The normality rule of Generalised Standard Materials [22] allows us to write the damage evolution as

$$\dot{D} = \begin{cases} \dot{\delta}\frac{\partial f}{\partial Y} & \text{if } f = 0 \text{ (damage evolves)} \\ 0 & \text{if } f < 0 \text{ or } D = D_\infty \text{ (damage remains constant)} \end{cases} \tag{16}$$

where $\dot{\delta}$ is the damage multiplier. Eq. (14) and Eq. (16) allow us to write $\dot{D} = \dot{\delta}$. The damage evolution $\dot{D}$ is deduced from the consistency condition ($\dot{f} = 0$) and from the damage condition ($f = 0$), so that

$$\dot{D} = \left\langle \frac{[\frac{\mathbf{S}^{\mathrm{iso}}}{2(1-D)} + [\frac{K_{\mathrm{v}}}{2}\tilde{J}^2\frac{g'(D)}{g(D)}]C^{-1}] : \dot{C}}{Q'(D) - [\frac{K_{\mathrm{v}}}{2}[-(\frac{g'}{g})^2(3\tilde{J}^2 - 1) + \frac{g''}{g}(\tilde{J}^2 - 1)]]} \right\rangle \tag{17}$$

where $\langle x \rangle$ denotes the positive value of x (this insures $\dot{D} \geqslant 0$ with the parameter $\eta > 0$), $g(D) = 1 + \alpha D$, $g' = \alpha$ and $g'' = 0$. Furthermore the dissipation Ω can be written as follows:

$$\Omega = \rho_O \frac{\partial W}{\partial \mathbf{E}} : \dot{\mathbf{E}} - \rho_O \frac{\partial W}{\partial A_{\mathrm{K}}}\dot{A}_{\mathrm{K}} = Y\dot{D} \tag{18}$$

where A_{K} are the internal and observable variables used in the model (D and $\mathbf{E}$). From Eq. (9) and Eq. (17), the dissipation Ω is always positive whatever the imposed load. The approach is thus thermodynamically acceptable as it verifies the Clausius–Duhem inequality. The model had seven material parameters that can be related to hyperelasticity ($C_{10}, C_{01}, C_{20}, K_{\mathrm{v}}$) and damage evolution ($\alpha, \eta, D_\infty$).

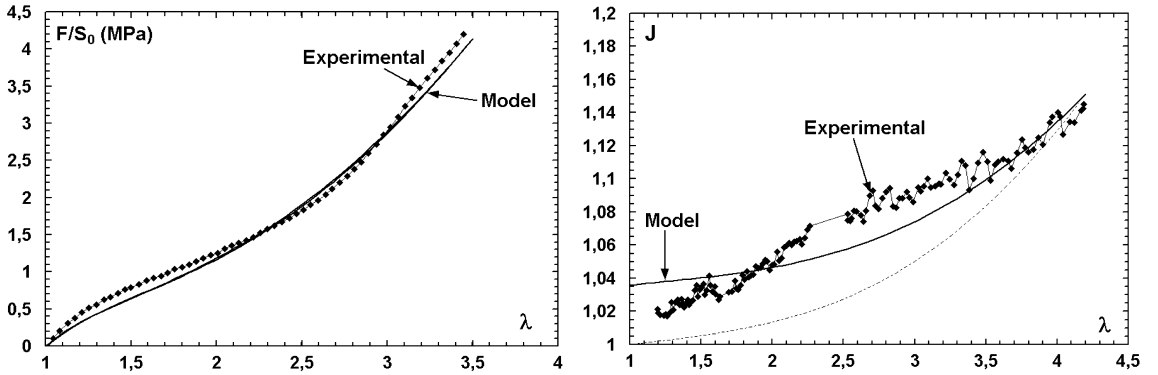

Fig. 10. Uniaxial test used for the model parameters identification. λ: elongation, F/S_0: engineering stress, $J = V/V_0$.

Table 3
Identified model parameters corresponding to NR-CB used in this study.

Coefficients	Values
C_{10} (MPa)	0.15
C_{01} (MPa)	0.2
C_{20} (MPa)	0.0235
K_v (MPa)	750
D_∞	0.5
η	3105
α	50

3.2. Numerical implementation of the model

The aforementioned constitutive equation has been implemented into the Z-set finite element (FE) code [23]. The global resolution is done by means of Newton–Raphson method [24]. The tangent matrix ($\underline{\underline{L}}$) is defined in Appendix A. The consistent tangent matrix $\underline{\underline{L}}_C$ used for the FE formulation is approached by the tangent matrix, so that $\underline{\underline{L}}_C \approx \underline{\underline{L}}$. Concerning damage evolution, Eq. (17) will be used in the case of formal calculation. In the FE calculation, the damage parameter will be integrated by applying a semi-implicit integration scheme to the damage condition $f = 0$. This is sufficient to ensure the consistency condition, as the model is associated. This is equivalent to solve Eq. (19) by introducing a residual scalar R as

$$R = R_D = Y - Q(D) = 0 \tag{19}$$

The solution $R = 0$ is searched with respect to the increment of the state variable D using an iterative Newton–Raphson method. The Jacobian, J_{ac}, of Eq. (19) is therefore required. It can be computed as

$$[J_{ac}] = \frac{\partial\{R_D\}}{\partial \Delta D} = \frac{\partial Y}{\partial D} - Q'(D) \tag{20}$$

where $\frac{\partial Y}{\partial D} = \frac{K_v}{2}[-(\frac{g'}{g})^2(3\tilde{J}^2 - 1) + \frac{g''}{g}(\tilde{J}^2 - 1)]$ is the hysteresis loop (Fig. 11).

3.3. Parameters identification and model abilities

The seven model parameters are fitted to the experimental stabilised material response under uniaxial tension in terms of stress–strain and volume–strain curves (Fig. 10). The obtained coefficients are reported in Table 3. Note that the value of K_v is lower than the bulk modulus experimentally determined under oedometric compression. This is due to the fact that the parameter K_v is optimised on the stabilised state and for low triaxiality loading.

The same model response calculated formally by Maple™ software and by FE Method has been obtained in the case of cyclic uniaxial tension. Thus, the FE implementation of the model is validated under cyclic uniaxial tension. Furthermore, the model response, compared to an incompressible one, reveals both stress softening and hysteresis loop (Fig. 11).

The evolution of volume change and damage under cyclic uniaxial tension is described in Fig. 12. Under loading, both damage and volume increase. During unloading, damage remains constant, whereas volume is partially restored. The evolution of volume during unloading represents the reversible part of volume change. The irreversible part increases with damage accumulation during loading history. So, during the following cycles, volume change remains identical to that after the first unloading, since there is no cyclic damage accumulation. The stabilised state can thus be defined as corresponding to a constant value of damage.

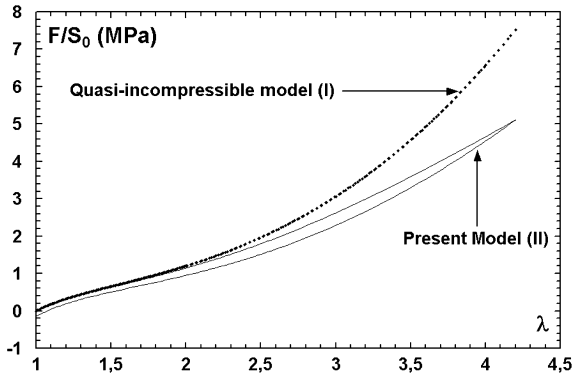

Fig. 11. Comparison between a Rivlin incompressible model (I: $C_{10} = 0.15$ MPa, $C_{01} = 0.2$ MPa, $C_{20} = 2.35 \times 10^2$ MPa, $K_v = 750$ MPa) and the damage-induced compressible approach (II: $C_{10} = 0.15$ MPa, $C_{01} = 0.2$ MPa, $C_{20} = 2.35 \times 10^2$ MPa, $K_v = 750$ MPa, $D_\infty = 0.5$, $\eta = 3104$, $\alpha = 50$).

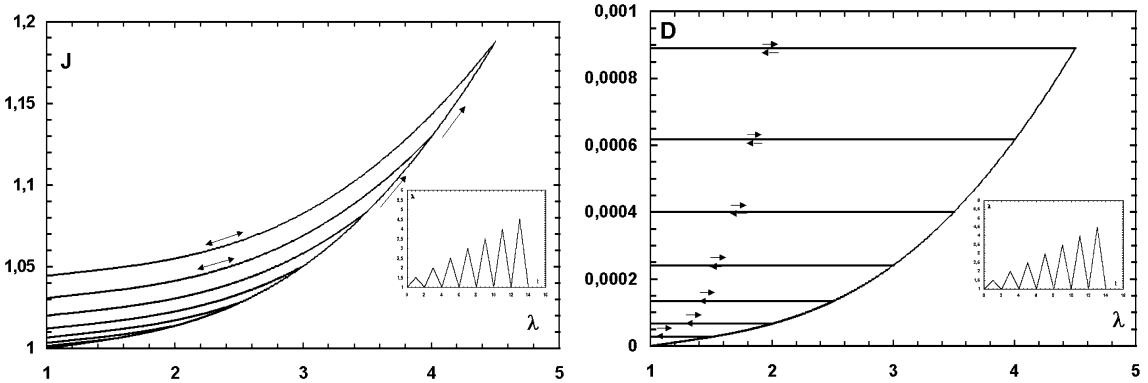

Fig. 12. Description of loading (l versus t), volume change (J) and damage (D) evolutions for cyclic uniaxial tensile test. The model parameters used are those of Table 3.

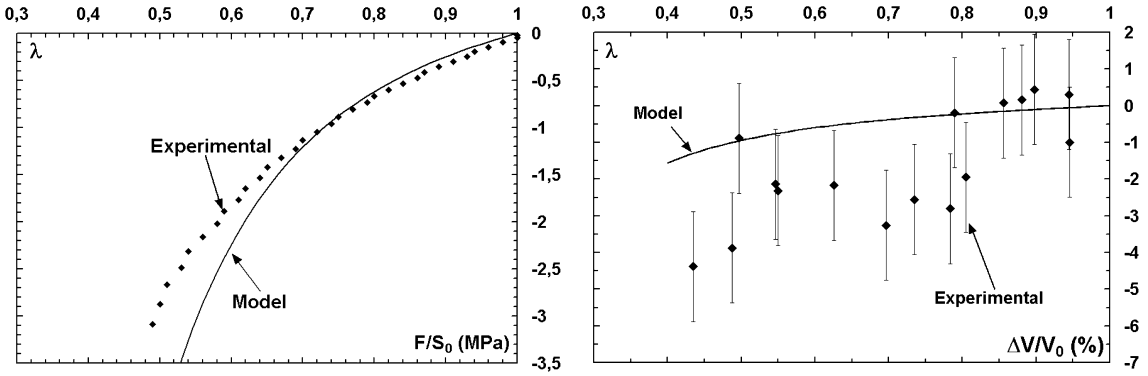

Fig. 13. Uniaxial compression test: comparison between model prediction (line) and experimental results (dots).

The parameter α controls the reversibilty part. The introduction of the parameter α is part of the originality of this model, if the value of α is choosen as $\alpha = 1$, the evolution of damage and volume change are the same and they are totally irreversible (see Saanouni's model [27]).

3.4. Model validation

The modelling approach was validated by comparing the model prediction to experimental results for the other loading conditions experimentally investigated.

First, under uniaxial compression, the stress response is well-predicted. In fact, the discrepancy between experimental and numerical response begins at elongation $\lambda = 0.65$, corresponding to barrelling (Fig. 13). Volume change is underestimated, but it is more realistic than that predicted using an incompressible approach.

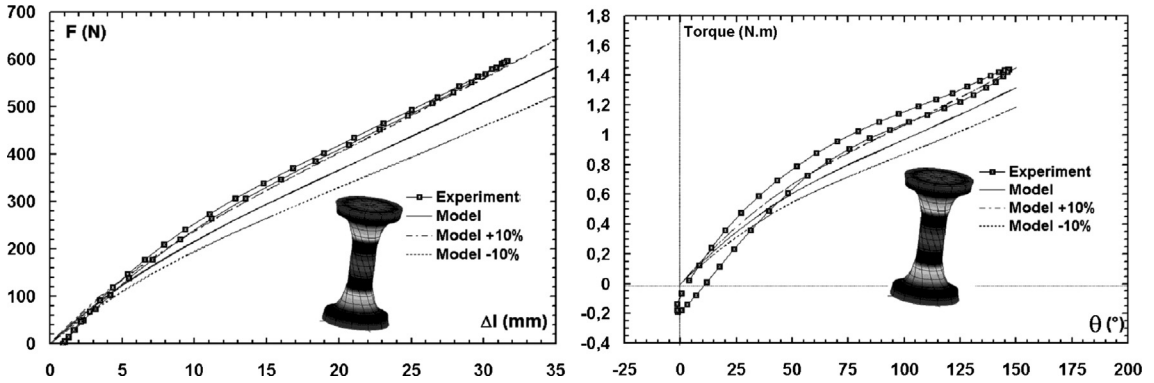

Fig. 14. Proportional tension–torsion test ($0 \leqslant F \leqslant 600$ N, $0 \leqslant \Theta \leqslant 150°$; F: axial force; Θ: twist angle): comparison between model prediction (lines) and experimental results (symbols).

Furthermore, the model has been validated for more complex loading conditions carried out on the same material. Experimental data obtained from Diabolo specimen loaded under in phase fatigue in tension–torsion–compression are considered. A 3D mesh containing 675 elements and 9318 degrees of freedom was used. Good agreement was obtained between experimental results and model predictions (Fig. 14). Satisfactory results were also obtained under out-of-phase loading.

4. Conclusions

Volume change has been studied and experimentally quantified under various loading conditions for a carbon black-reinforced natural rubber. The experimental results show a significant volume change and are in contradiction with the commonly adopted assumption of incompressible material. At the microscopic scale, volume change under uniaxial tension is due to the decohesion between ZnO particles and the elastomeric matrix. Volume change is triaxiality dependent and can be either reversible or not, depending on the interactions between damage, stress softening and crystallisation. Applied to multi-scale microstructure model of carbon black distribution in rubber [25,26], our results appear to be helpful in order to understand the link between volume fraction and damage such as the Mullins effect. Furthermore, the cavitation mechanism occurring under uniaxial tension is different from that occurring under hydrostatic tension. In fact, ZnO particles are responsible for uniaxial cavitation, but they do not participate in crack initiation, whereas under hydrostatic conditions cavitation observed under monotonic loading occurs in high-triaxiality zones (independently of ZnO particles) and can lead to the specimen's rupture.

Based on the experimental results, damage-induced compressibility was modelled. A phenomenological approach was chosen within a hyperelastic nearly compressible framework. Good agreement between experimental results and model predictions was obtained for low-triaxiality loading conditions.

Acknowledgements

The authors gratefully acknowledge the experimental support of Hutchinson France and particularly M. Pompei and K. Legorju for many helpful discussions on the experimental aspects of this work.

Appendix A. Tangent matrix calculation

The tangent matrix $\underline{\underline{L}}$ is defined as

$$\dot{\mathbf{S}} = \underline{\underline{L}} : \dot{\mathbf{E}} \tag{21}$$

where $\mathbf{S} = \mathbf{S}(\mathbf{C}, D) = \mathbf{S}(\mathbf{E}, D)$. So

$$\mathbf{S} = \frac{\partial \mathbf{S}}{\partial \mathbf{E}} : \dot{\mathbf{E}} + \frac{\partial \mathbf{S}}{\partial D}\dot{D} = \underbrace{2\frac{\partial \mathbf{S}}{\partial \mathbf{C}}}_{\text{Hyperelastic part}} : \dot{\mathbf{E}} + \underbrace{2\frac{\partial \mathbf{S}}{\partial D} \otimes \frac{\partial D}{\partial \mathbf{C}}}_{\text{Damageable part}} : \dot{\mathbf{E}} = \underline{\underline{L}}_{\text{hyper}} : \dot{\mathbf{E}} + \underline{\underline{L}}_{\text{damage}} : \dot{\mathbf{E}} \tag{22}$$

where $\underline{\underline{L}}_{\text{hyper}}$ and $\underline{\underline{L}}_{\text{damage}}$ are fourth-order tensors.

The expression of $\underline{\underline{L}}_{\text{damage}}$ is given by Eq. (23).

$$\underline{\underline{L}}_{\text{damage}} = -4\left[I_3^{-1/3}\frac{\partial W_0}{\partial \bar{I}_1}\frac{\partial I_1}{\partial \mathbf{C}} \otimes \frac{\partial D}{\partial \mathbf{C}} + I_3^{-2/3}\frac{\partial W_0}{\partial \bar{I}_2}\frac{\partial I_2}{\partial \mathbf{C}} \otimes \frac{\partial D}{\partial \mathbf{C}}\right] - 2K_v\frac{g'}{g^3}\left(\frac{\partial I_3}{\partial \mathbf{C}} \otimes \frac{\partial D}{\partial \mathbf{C}}\right) \tag{23}$$

The expression of $\partial D/\partial \mathbf{C}$ is derived from the consistency condition $\dot{f}=0$, so that

$$\frac{\partial D}{\partial \mathbf{C}} = -\frac{(\frac{\partial f}{\partial \mathbf{C}})}{(\frac{\partial f}{\partial D})} \tag{24}$$

where $\frac{\partial f}{\partial D} = -K_{\mathrm{v}}(g')^2\frac{(3\tilde{J}^2-1)}{2g^2} - \frac{\eta}{D_\infty - D}$

$$\frac{\partial f}{\partial \mathbf{C}} = \frac{\partial Y}{\partial \mathbf{C}} = \frac{\mathbf{S}^{\mathrm{iso}}}{2(1-D)} + \left[\frac{K_{\mathrm{v}}}{2}\frac{g'\tilde{J}^2}{g}\right]\mathbf{C}^{-1}$$

References

[1] W.F. Busse, Physics of rubber as related to the automobile, J. Appl. Phys. 9 (1938) 438.
[2] F.L. Yerzley, Adhesion of neoprene to metal, Ind. Eng. Chem. 31 (1939) 950–956.
[3] A.N. Gent, P.B. Lindley, Internal rupture of bonded rubber cylinders in tension, Proc. R. Soc. A 249 (1958) 195–205.
[4] A.N. Gent, D.A. Tompkins, Nucleation and growth of gas bubbles in elastomers, J. Appl. Phys. 40 (1969) 2520–2525.
[5] K. Cho, A.N. Gent, Cavitation in model elastomeric components, J. Mater. Sci. 23 (1988) 141–144.
[6] A.N. Gent, C. Wang, Physics of rubber as related to the automobile, J. Appl. Phys. 9 (1990) 3392–3395.
[7] S.L. Burtscher, A. Dorfmann, Experimental and computational aspects of cavitation in natural rubber, in: A. Dorfmann, A. Muhr (Eds.), Constitutive Models for Rubber, Balkema, Rotterdam, The Netherlands, 1999, pp. 201–209.
[8] A. Dorfmann, R.W. Ogden, Stress softening in rubber-like solids subjected to cavitation damage, in: D. Besdo, R.H. Schuster, J. Ihlemann (Eds.), Constitutive Models for Rubber II, 2001, pp. 193–203.
[9] A. Dorfmann, K.N.G. Fuller, R.W. Ogden, Shear, compressive and dilatational response of rubber-like solids subject to cavitation damage, Int. J. Solids Struct. 39 (2002) 1845–1861.
[10] A.N. Gent, Crystallization and the relaxation of stress in stretched natural rubber vulcanizates, Trans. Faraday Soc. 50 (1954) 521–533.
[11] N. Bekkedahl, Forms of rubber as indicated by temperature–volume relationship, J. Res. Natl. Bur. Stand. 13 (1934) 410.
[12] L.A. Wood, N. Bekkedahl, Crystallization of unvulcanized rubber at different temperatures, J. Appl. Phys. 17 (1946) 362–375.
[13] Y. Pannier, H. Proudhon, C. Mocuta, D. Thiaudière, S. Cantournet, In situ multiaxial loading frame to probe elastomers using X-ray scattering, J. Synchrotron Radiat. 18 (2011) 907–911.
[14] C. G'Sell, J.-M. Hiver, A. Dahoun, Experimental characterisation of deformation damage in solid polymers under tension and its interrelation with necking, Int. J. Solids Struct. 39 (2002) 3857–3872.
[15] K. Le Gorju Jago, X-ray computed microtomography of rubber, Rubber Chem. Technol. 85 (3) (2012) 387–407.
[16] K. Layouni, S. Cantournet, L. Laiarinandrasana, R. Piques, Compressibility induced by damage in carbon black reinforced natural rubber, in: ECCMR IV, Proceedings of the Fourth Conference on Constitutive Models for Rubber, 2007.
[17] F. Andrieux, Sur les milieux visco-hyperélastiques endommageables, Ph.D. thesis, Université de technologie de Compiègne, France, 1996 (in French).
[18] P.J. Flory, Thermodynamic relations for high elastic materials, Trans. Faraday Soc. 57 (1961) 829–838.
[19] J.C. Simo, R.L. Taylor, Quasi-incompressible finite elasticity in principal stretches. Continuum basis and numerical algorithms, Comput. Methods Appl. Mech. Eng. 85 (1991) 273–310.
[20] R.W. Penn, Volume changes accompanying the extension of rubber, Trans. Soc. Rheol. 40 (4) (1970) 509–517.
[21] D. Doll, K. Schweizerhof, On the development of volumetric strain energy functions, J. Appl. Mech 67 (2000) 17–21.
[22] P. Germain, Q.S. Nguyen, P. Suquet, Continuum thermodynamics, J. Appl. Mech. 105 (1983) 1010–1020.
[23] J. Besson, R. Foerch, Large scale object-oriented finite element code design, Comput. Methods Appl. Mech. Eng. 142 (1997) 165–187.
[24] J. Besson, G. Cailletaud, J.-L. Chaboche, S. Forest, Mécanique non linéaire des matériaux, Hermès Science Publications, Paris, 2001 (in French).
[25] A. Jean, S. Forest, F. Willot, S. Cantournet, D. Jeulin, Large-scale computations of effective mechanical properties of rubber with carbon black fillers, Int. J. Multiscale Comput. Eng. 9 (3) (2011) 271–303.
[26] A. Jean, D. Jeulin, S. Forest, S. Cantournet, F. N'Guyen, A multi-scale microstructure model of carbon black distribution in rubber, J. Microsc. 241 (3) (2011) 243–260.
[27] K. Saanouni, F. Sidoroff, F. Andrieux, Damage hyperelastic solid with an induced volume variation. Effect of loading paths, in: G.Z. Voyiadjis, J.W. Ju, J.-L. Chaboche (Eds.), Damage Mechanics in Engineering Materials, Elsevier, 1998, pp. 503–522.
[28] N. Saintier, Prévision de la durée de vie en fatigue du NR, sous chargement multiaxial, Ph.D. thesis, École nationale supérieure des mines de Paris, Paris, France, 2001 (in French).